JOURNAL OF NEUROTRAUMA 37:494–506 (February 1, 2020)

DOI: 10.1089/neu.2019.6540

Spinal Cord Injury Results in Chronic Mechanical Stiffening

John G. Cooper,[1,*] Delphine Sicard,[2,*] Sripadh Sharma,[1] Stephanie Van Gulden,[1] Tammy L. McGuire,[1] Miguel Pareja Cajiao,[3] Daniel J. Tschumperlin,[2] and John A. Kessler[1]

Abstract

Gliosis and fibrosis after spinal cord injury (SCI) lead to formation of a scar that is thought to present both molecular and mechanical barriers to neuronal regeneration. The scar consists of a meshwork of reactive glia and deposited, cross-linked, extracellular matrix (ECM) that has long been assumed to present a mechanically ''stiff'' blockade. However, remarkably little quantitative information is available about the rheological properties of chronically injured spinal tissue.

In this study we utilize atomic force microscopy microindentation to provide quantitative evidence of chronic mechanical stiffening after SCI. Using the results of this tissue characterization, we assessed the sensitivity of both mouse and human astrocytes *in vitro* and determined that they are exquisitely mechanosensitive within the relevant range of substrate stiffness observed in the injured/uninjured spinal cord. We then utilized a novel immune modifying nanoparticle (IMP) treatment as a tool to reveal fibrotic scarring as one of the key drivers of mechanical stiffening after SCI *in vivo*. We also demonstrate that glial scar-forming astrocytes form a highly aligned, anisotropic network of glial fibers after SCI, and that IMP treatment mitigates this pathological alignment. Taken together, our results identify chronic mechanical stiffening as a critically important aspect of the complex lesion milieu after SCI that must be considered when assessing and developing potential clinical interventions for SCI.

Keywords: fibrotic scar; immune modifying nanoparticles; mechanical properties; spinal cord injury; stiffness

Introduction

Spinal cord injury (SCI) often results in permanent loss of motor and sensory function below the injury site. The failure to recover reflects the inability of damaged axons to re-grow across the injury site and rewire correctly. The failure of axon re-growth and functional recovery after SCI has long been attributed to the chronic scar that forms at the site of injury. This scar is composed of both glial and fibrotic components that present both molecular and mechanical barriers to neuronal regeneration.[1,2] The molecular barrier results from accumulation of molecules that inhibit axonal regeneration.[3,4] The physical barrier consists of a meshwork of reactive glia and deposited, cross-linked, extracellular matrix (ECM). The mechanical properties that limit axon re-growth through the scar are largely unknown, and there is no consensus about the rheological environment within spinal lesions. This is a critical gap in our understanding of the pathophysiology of SCI because an ever-increasing number of studies have demonstrated that both glia and neurons are exquisitely mechanosensitive.

Transmembrane proteins such as integrins expressed by neurons and glia bind to the ECM and mechanically couple the cytoskeleton to the environment. This allows cells to sense and respond to the stiffness of the substrates they encounter, facilitating cell growth, migration, and spreading.[5] Rat astrocytes plated on stiffer substrates *in vitro* spread more and develop more complex shapes than astrocytes on soft substrates.[6] Conversely, mouse spinal cord neurons plated on softer substrates display enhanced neurite branching[7] and dorsal root ganglia neurite extension in three dimension (3D) is blocked by interfaces with stiffer gel substrates.[8] Mixed cultures of murine neurons and astrocytes grown together on soft substrates with stiffnesses comparable to brain tissue ($\sim$200 Pa) select for preferential growth of neurons, whereas stiffer substrates cause astrocytes to overgrow neurons.[9] Collectively, these studies suggest that the rheological environment of the lesion provides important mechanical cues that affect glial activation and/or neuronal regeneration after SCI.

As long ago as the early 1950s some investigators hypothesized that the spinal scar may present a mechanically stiff blockade to regenerating axons.[6,8,10] However, a number of groups have published evidence rejecting the idea of mechanical stiffening after SCI. Moeendarbary et al. reported that spinal cord crush injury in rats leads to tissue softening at acute and subacute time-points ($\sim$7 and 21 days post-injury).[11] A 2012 study by Saxena et al. assessed the injured rat spinal cord at more chronic time-points and reported

[1]Department of Neurology, Northwestern University Feinberg School of Medicine, Chicago, Illinois.
[2]Department of Physiology and Biomedical Engineering, [3]Department of Anesthesiology, College of Medicine and Science, Mayo Clinic, Rochester, Minnesota.
*The first two authors contributed equally.

that the tissue exhibited lower elastic modulus after a spinal hemisection injury.[12] These studies challenge the idea of spinal tissue stiffening after injury, and, to our knowledge, no study has provided quantitative examination and confirmation of an SCI-induced stiffening phenomenon.

In this study we use atomic force microscopy (AFM) micro-indentation to evaluate the micromechanical properties of spinal cord and demonstrate that the chronically injured mouse spinal cord is indeed stiffer than healthy tissue. We then determine that glial cells from both mouse and human sources respond to changes in substrate stiffness within the biological range of injured/uninjured spinal tissue. Finally, we use a nanoparticle-based therapy to inhibit fibrotic scar formation and demonstrate that the pathological stiffening of spinal cord tissue after injury is due to the presence of the chronic spinal scar.

Methods

Experimental design

The present work adheres to the ARRIVE guidelines for reporting animal research.[13] The objective of this study was to study the mechanical properties of the chronically injured spinal cord and to determine whether reducing fibrotic scarring through treatment with immune modifying nanoparticles (IMP) alters pathological tissue stiffening after SCI in mice.[14]

Mouse spinal cord injury and animal care

All animal procedures were approved by the Northwestern University Institutional Animal Care and Uses Committee and adhered to the Public Health Service Policy on Humane Care and Use of Laboratory Animals. Animals were housed in the Northwestern University Center for Comparative Medicine and cared for according to its standard operating procedures. SCI was performed using the Infinite Horizons Spinal Cord Impactor system (IH-0400, Precision Systems and Instrumentation). A severe injury paradigm was used, with 100 kdyn of impact force and a dwell time of 60 seconds to make a severe T11 contusion SCI to mice. These conditions are identical to those used in our previous publication on IMP.[14] Eight-weeks-old female C57BL/6 wild-type mice (Charles River Labs) were used for all SCI experiments. ''Sham'' control animals were anesthetized and the paraspinal muscles dissected, but no laminectomy was performed. Post-operational care was performed as previously described.[14,15] Buprenorphine anesthetic (0.05 mg/kg, subcutaneously in 1 mL sterile saline) was administered daily for 2 days after injury. Baytril antibiotic (2.5 mg/kg, subcutaneously in 1 mL sterile saline) was administered daily for 3 days after injury to reduce the risk of infection. Bladders were manually expressed daily.

IMP treatment

Biodegradable carboxylated poly(lactide-*co*-glycolide) (PLG) IMP (500 nm diameter) were obtained from Phosphorex, Inc. (Fall River, MA) and diluted in sterile isotonic 0.9% saline (Ricca) to a final concentration of 4.7 mg/mL. 200 μL of dilute IMP solution was injected via tail vein 2 h after SCI. Subsequent injections were performed at 24 and 48 h post-injury. Treatment was randomized by cage. Control injured animals received equivalent volume injections of sterile saline at the same time-points. No adverse events were observed in connection with IMP or saline treatment.

Dissection and preparation of spinal cord tissue

At 12 weeks post-SCI (12 WPI), mice were euthanized via CO_2 inhalation and perfused with 20 mL ice-cold phosphate-buffered saline (PBS). Spinal cords were quickly dissected and snap frozen. Tissue samples were stored at −80°C until they were shipped on dry ice from the Kessler lab to the Tschumperlin lab. Spinal cords were embedded in Tissue-Plus O.C.T. Compound (optimal cutting temperature) (Fisher HealthCare) and then frozen in dry-ice-cooled 2-methylbutane and stored at −80°C. Transverse sections of spinal cord (10 μm thick) were cut on a Leica CM1860 UV cryostat, mounted on poly-L-lysine-coated glass slides (Electron Microscopy Sciences), and stored at −80°C. To perform AFM measurements, glass slides with tissue sections were placed in plastic Petri dishes (15 mm diameter, Corning) for about 15 min with droplets of water surrounding them, to thaw slowly to room temperature while also maintaining high humidity to avoid tissue drying. Once defrosted, PBS solution was added to the tissue slices and adequate hydration was maintained throughout AFM characterization. We will refer to this method of sample preparation as the ''frozen/thawing tissue process.''

The ''fresh tissue process'' for spinal cord sample preparation has been adapted from Koser et al.[17] Spinal cords were harvested from two uninjured adult (30 weeks old) female C57BL/6 wild-type mice. One segment of spinal cord was embedded in 4% low melt agarose (Roche) at 37°C and kept on ice to rigidify the agarose. From this agarose-embedded sample, fresh transverse sections of tissue were cut at 500 μm thickness in PBS by vibratome (Precisionary Instruments, Inc.). Tissue slices were then mounted on glass slides previously coated with Cell-Tak adhesive (Corning). Samples were kept on ice in plastic Petri dishes (15 mm diameter, Corning) for 15 min to complete tissue adhesion, with PBS on the top to avoid tissue drying. In total, the procedure from sacrifice to fresh tissue analysis by AFM was carried out within approximately 2 h. To compare the mechanical properties of spinal cord tissue prepared with these two processes, adjacent segments of spinal cord were dissected from the same mice and preserved in parallel using our frozen/thawing tissue process for analysis.

Experimental optimization for AFM microindentation

To assess the micromechanical properties of mouse spinal cord by AFM microindentation, we developed the following experimental protocol (Fig. 1A). Areas of interest in thin sections of spinal cord tissue were identified under phase contrast microscope (200×) (Olympus). Microindentation force curves were performed by AFM on each area of interest in PBS at room temperature using a Catalyst Bioscope atomic force microscope (Bruker) and a 2.5 μm radius borosilicate sphere AFM tip (Novascan). The spring constant k of AFM tips was estimated at 100 pN/nm by thermal tune.[17] MIRO 2.0 software was used through Nanoscope 9.1 (Bruker) to operate microindentation. The Young's modulus (elastic modulus) was then estimated by fitting each force curve (NanoScope Analysis 1.8 software, Bruker) using the Hertz contact model for spherical indenter[18–20] and following the relationship:

$$E = \frac{3}{4}\frac{(1-\nu^2)}{R^{1/2}\delta^{3/2}}F \qquad \text{Eq.(1)}$$

with R the tip radius, v the Poisson's ratio assumed at 0.5 for spinal cord tissue,[12] and δ the sample indentation.

One important consideration in evaluating the stiffness of soft biological tissues, such as spinal cord, is that the force applied during tissue indentation and the determination of the point of contact must be carefully selected to avoid over- or under-estimation of elastic modulus. When the force curve is performed (graphically represented by the force F as a function of the tip displacement Z-Displacement, Fig. 1A), the AFM system progressively advances the AFM tip toward the sample until a defined value of force is applied. During this process, the tip comes in contact with the tissue (called contact point) and indents it. The force applied on the tissue should be adjusted to avoid experimental

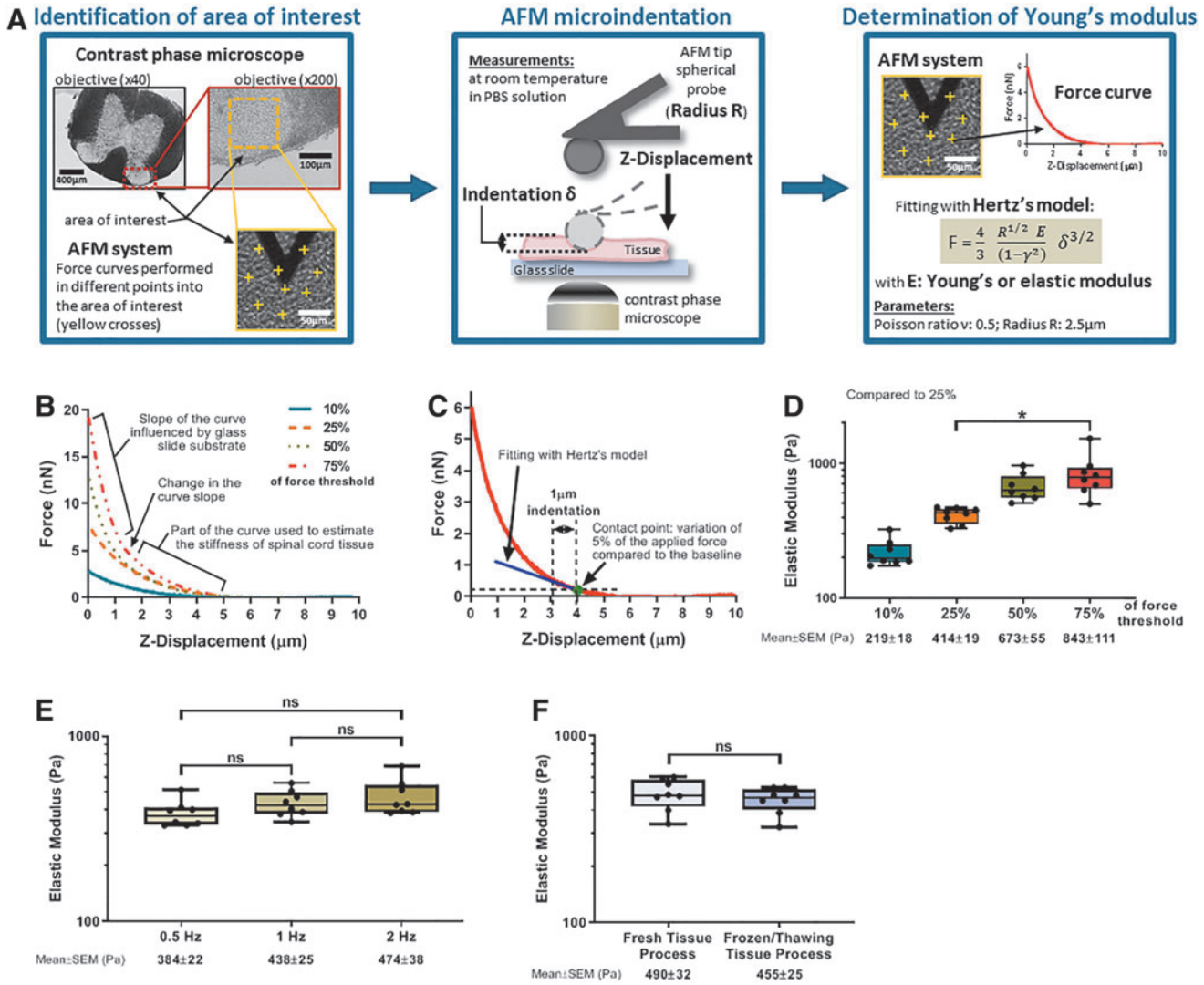

FIG. 1. Determination of AFM experiment and data analysis parameters, and sample preparation to characterize mouse spinal cord stiffness. **(A)** Schematic description of AFM microindentation experiment from the identification of area of interest on mouse spinal cord tissue to the determination of the elastic modulus. **(B)** Representative force curves performed on mouse spinal cord tissue (from control uninjured mouse spinal cord, 12 weeks post-sham injury) at an applied force corresponding to 10, 25, 50, and 75% of the maximal force threshold. **(C)** Schematic explanation of the determination of contact point and Hertz's model fitting on a force curve performed on control spinal cord tissue. Mean elastic modulus ± SEM of control uninjured mouse spinal cord samples (white and gray matter areas combined) from AFM measurements performed at 10, 25, 50, and 75% of the force threshold **(D)** and at 0.5 Hz, 1 Hz, and 2 Hz of loading rate **(E)**. In (D), statistical results are presented considering values at 25% as a reference and with significance at $*p < 0.05$. All statistical results are shown in Supplementary Table S1 and Supplementary Table S2. **(F)** There was no significant difference between the elastic moduli of uninjured mouse spinal cords prepared using the ''fresh'' and ''frozen/thawing'' processes. In box and whisker plots, the box indicates the 25th and 75th percentiles of the values, the line inside the box is the median value, and the whiskers the smallest and largest values. Markers represent the average of 10 force curves performed per area. In total, two control uninjured mouse spinal cords samples were analyzed with two areas (white and gray matter) per slice and two non-consecutive slices per animal. Statistical analysis of the elastic modulus values using Kruskal-Wallis test (multiple comparisons) (D,E) and Mann-Whitney test (F). AFM, atomic force microscopy; SEM, standard error of the mean.

noise and the misidentification of the contact point in the case of too low force,[21–23] and to prevent the damage of the sample and the underlying hard substrate in the case of too high force.[24,25]

With the aim of defining the appropriate force that should be applied to spinal cord tissue, force curves were performed on uninjured spinal cord sample (sham, on white and gray matter areas), with force values corresponding to 10, 25, 50, and 75% of the maximal force threshold allowed by the AFM system (corresponding to ~2.8, 7.8, 13.2, and 19.4 nN based on a force threshold of 26.4 nN). This force threshold value depends on the sensitivity of photodiode and the spring constant of cantilever. Representative force curves are shown in Fig. 1B. Between 4 and 5 μm of Z-displacement, we observed a progressive increase of the force indicating the contact between the sample and the AFM tip (decreasing Z indicates movement closer to the sample). From this contact point, the slope of the force curve reflects the mechanical properties of the tissue sample. Between 1 and 2 μm of Z-displacement, a change of slope is noted, in particular in the 25,

50, and 75% maximal force threshold curves (Fig. 1B). This change in slope is consistent with a second distinct mechanical behavior likely caused by an effect of the underlying rigid glass substrate when the tissue indentation is over 30% of the tissue thickness (tissue slice cut at 10 μm thickness).

For soft tissue, the contact point can be difficult to determine accurately and depends on the judgment of the experimenter and/or data analysis software. To avoid misidentification and considering the low force variation, a contact point threshold has been determined relative to the force applied on a sample. The contact point is defined when the force reaches a value corresponding to 5% of the applied force (Fig. 1C). As an example, if the force curve is performed at 6 nN as the final applied force, the contact point is at 0.3 nN.

From this contact point, the fitting of the force curve by spherical Hertz's model is used to estimate the elastic modulus.[18–20] In the Hertz theory on the deformation of two bodies in contact under load, the mathematical model is based on the assumption that the tissue section is an infinite half-space.[18–20] Experimentally, all tissue samples have a finite thickness, which is a violation of the assumption. In the literature, several studies have demonstrated the effect of thin finite thickness on elastic modulus values and proposed some corrective factors to re-adjust the hertzian indentation model in case of one or several violating assumptions.[18,26–28] In our study, to be close to Hertz's assumptions, the Hertz model fitting has been restricted to the first micron of indentation from the contact point, as shown in Figure 1C. This 1 μm indentation represents 10% of the tissue thickness (tissue slices cut at 10 μm thickness), as usually recommended in the literature,[21,25,28] and also minimizes the effect of the underlying hard substrate.

In Figure 1D, the mean elastic values of uninjured spinal cord tissue measured from two uninjured mice are represented as a function of the applied force (percentage relative to the maximal force threshold). Each marker in the graph is the mean Young's modulus value of 10 force curves performed in the area of interest. In total, two areas were analyzed per slice and two non-consecutive tissue slices (cut at 10 μm thickness) per animal. The elastic modulus increases at the same time that the force applied on the sample goes up with a significant difference in some cases, as between values at 25% compared with 75% of force threshold for example (see full statistical results in Supplementary Table S1). The mechanical change observed on force curves in Figure 1B could explain this difference.

For measurements taken at 10% of force threshold, elastic modulus is around 219 Pa, which is 2 times lower than values found for 25% of force threshold (414 Pa) but with no statistically significant difference (Supplementary Table S1). To respect the Hertz model and the assumption of infinitesimal strains, small loads are recommended, but unfortunately they can lead to low signal-to-noise ratios.[28] Based on these observations, our AFM microindentation experiments on mouse spinal cord tissue in the remainder of this study were performed using a 25% maximum force threshold (corresponding to $\sim$5–7 nN) to avoid experimental noise (may be the case at 10% maximum force threshold) and the influence of the hard substrate (observed for 50% and 75% maximum force threshold, Fig. 1B).

To investigate the loading rate effect, force curves were performed on mouse spinal cord tissue at 0.5, 1, and 2 Hz, representing a speed rate of 10, 20.6, and 41.1 μm/s respectively for a ramp size of 10 μm. Elastic modulus values from 10 force curves were averaged per area (Fig. 1E). Two different areas were analyzed per tissue slice and two non-consecutive slices were considered per animal for a total of two mice (uninjured animal group) included in this AFM parameter study. Li et al. have demonstrated for cells the dependence of Young's modulus on the loading rate due to the contribution of cell viscosity.[29] In our study on spinal cord tissue, we did not observe any significant relationship between the elastic modulus and the loading rate (Fig. 1E and Supplementary Table S2). For all following AFM experiments in this study, the scan rate was set at 1 Hz.

A recently published study by Vishwakarma et al. demonstrated that sample cryopreservation does not affect the structural organization and the ECM composition of meningeal tissue.[30] However, to verify that a single sample freeze-thaw cycle is not excessively disruptive to the mechanical properties of the tissue being measured, we have compared our frozen/thawing tissue process with a fresh tissue process adapted from Koser et al.[16] From the same uninjured spinal cords, two consecutive transverse segments were prepared using the frozen/thawing tissue process and the fresh tissue process, and both samples were analyzed by AFM in parallel. Spinal cord stiffness was not significantly different between these two sample preparation processes (Fig. 1F, $p = 0.3823$). Experiments on the stiffness of injured mouse spinal cord in the remainder of this study were performed using cryopreserved tissue samples.

In total, we analyzed three different tissue sections per mouse and four mice per condition: control/sham (uninjured spinal cords, 12 weeks post-sham injury; Sham 1–4), injured with saline vehicle treatment (saline-treated injured spinal cords,12 WPI; Saline 1–4), and injured with IMP treatment (IMP-treated injured spinal cords, 12 WPI; IMP 1–4). For each tissue section and condition, two different areas of interest were considered: gray and white matter for uninjured samples, and lesion core and rim for injured samples. Finally, 25 force curves at different points were performed in each area.

AFM microindentation measurements also were used to create stiffness maps to study the spatial distribution of spinal cord stiffness. Taking into account the AFM piezo system limitation (150×150 μm^2 maximum), 64 force curves were performed in a grid pattern using MIRO 2.0 software to complete a map of 8×8 pixels with a space of 11–15 μm between each point. The final stiffness maps have spatial dimensions between 90×90 μm^2 and 120×120 μm^2. Dimensions of all stiffness maps are indicated in Supplementary Table S3. The color maps were made using Prism software (heat map, version 8.0.1) with every color representing the actual elastic modulus value measured on that tissue slice. The scale bar has a gradient of color from blue for the lowest elastic values (200 Pa) to red for the highest values (11,000 Pa) and intermediate values in yellow (approximately 600 Pa).The elastic modulus values determined during the stiffness map experiments were not used to compare injured animal groups with the controls.

Immunohistochemistry

Mice were euthanized via CO_2 inhalation and transcardially perfused with ice-cold PBS followed by 4% paraformaldehyde (PFA) in PBS. Spinal cords were removed and post-fixed for 2 h in 4% PFA on ice. Samples were dehydrated overnight in 30% sucrose at 4°C and then embedded in O.C.T. compound. Embedded tissues were sectioned into 20-μm thick sagittal sections on a Leica CM3050S cryostat and collected onto gelatin subbed microscope slides (Fisher Scientific). Slides were washed in PBS-T (0.05% Triton X-100), blocked for 2 h in blocking media (5% normal goat serum in PBS-T), and incubated with primary antibodies at 4°C overnight in blocking media. Primary and secondary antibodies used are listed in Supplementary Table S4. Stained sections were mounted in ProLong Gold (Molecular Probes) and images were acquired with a Leica SP5 AOBS confocal microscope. Large format images were stitched using the native Leica Application Suite - Advanced Fluorescence software.

Mouse astrocyte cultures

Timed pregnant C57BL/6 wild-type dams were provided by Charles River. Astrocyte monolayer cultures were prepared from the cortices of post-natal day 2 pups.[31] Neonates were decapitated, brains were extracted, and the meninges carefully removed. The neocortex was isolated, washed in sterile Dulbecco's PBS (DPBS; Corning), triturated, and plated on tissue culture treated flasks

(Corning) in Dulbecco's Modified Eagle's Medium (DMEM)/F12 (Gibco) supplemented with 10% fetal calf serum (Hyclone) and 1 × penicillin, streptomycin, and L-glutamine (Invitrogen). Media were changed the day after plating and every 4 days thereafter. When cells became confluent (approximately 10 days), the flasks were sealed and shaken overnight at 225 RPM, 37°C to remove oligodendroglia. The following day, the remaining astrocyte monolayers were washed in sterile DPBS (Corning), treated with 0.25% trypsin-ethylenediaminetetraacetic acid (EDTA) (Gibco), and passaged onto fresh tissue culture flasks. All experiments described in this article were performed immediately after the second passage (P2).

Before use for rigidity experiments, CytoSoft variable elastic modulus plates (Advanced BioMatrix) and control plastic plates were coated with poly-D-lysine (PDL) according to the manufacturer suggested protocol. Briefly, 1 mg/mL PDL stock (Millipore) was diluted 1:50 in warm, sterile DPBS to create a working PDL concentration of 20 μg/mL. 3 mL of the PDL solution was added to each well and incubated for 1 h at room temperature. Newly coated wells were then washed twice with warm culture medium before use. CytoSoft plates use a 500 μm thick biocompatible silicone coating to produce a culture surface with a certified elastic modulus. The CytoSoft silicone coating is uniformly functionalized with an anhydride group to ensure efficient and homogeneous protein coating.[32] Each lot of CytoSoft plates is independently tested by the manufacturer to ensure that the elastic modulus of the culture surface falls within quality control tolerances.[33] We used 200 Pa and 2000 Pa plates in our experiments.

Human embryonic stem cell-derived astrocyte cultures

The H7 human embryonic stem cell (hESC) line was maintained on Matrigel (Corning) coated six-well plates in mTeSR1 (STEMCELL Technologies) medium. The medium was changed every day and the cells were passaged every 5–7 days using ReleSR (STEMCELL Technologies) following the manufacturer's instructions. For astroglial differentiation, H7 hESCs were dissociated using Accutase (Millipore) and plated as single cells on Matrigel or on poly-L-ornithine (PLO) (15 μg/mL; Sigma)/Laminin (10 μg/mL; Roche) double-coated culture vessels at a density of 200,000 to 250,000 cells/cm^2 in STEMdiff Neural Induction Medium (NIM) (STEMCELL Technologies) supplemented with 10 mol/L ROCK Inhibitor Y-27632 (Stemgent) for 24 h. Medium was replaced daily, and cells were passaged after 7 days using Accutase.

After the first passage, neural progenitor cells (NPCs) were passaged once they reached 70–80% confluency and plated at a density between 125,000 and 200,000 cells/cm^2. At passage 3, the medium was switched to STEMdiff Neural Progenitor Medium (NPM) (STEMCELL Technologies). From this point onward, the cells were passaged every 7 days using Accutase and the medium was replaced every other day. At passage 5, the NPCs were either cryopreserved in STEMdiff Neural Progenitor Freezing Medium (STEMCELL Technologies) and stored in liquid nitrogen for future use or re-suspended in STEMdiff Astrocyte Differentiation Medium and plated in either Matrigel or PLO/Laminin at a density of 100,000 cells/cm^2. At passage 7, the astrocyte precursors generated were matured using STEMdiff Astrocyte Maturation Medium (AMM) (STEMCELL Technologies) and maintained in AMM thereafter. Before plating the astrocytes (passages 9–12) in the CytoSoft plates, the cells were adapted to poly-D-Lysine (Millipore) for 7 days. For rigidity experiments, the same procedure outlined above in the ''Mouse astrocyte cultures'' section was used.

Immunocytochemistry of cultures

Astrocyte cultures were washed with sterile PBS and fixed with 4% PFA for 20 min directly on the CytoSoft plates. Fixed cells were washed in PBS-T (0.05% Triton X-100) and incubated with primary antibodies at 4°C overnight in blocking media (5% normal goat serum in PBS-T). Primary and secondary antibodies used are listed in Supplementary Table S4. Stained wells were mounted with ProLong Gold (Molecular Probes). Images were acquired with a 20 × LD objective on a Zeiss Axiovert 200 m epifluorescence microscope. Cells were quantified in 10 fields from each well. Quantification of astrocyte cell morphology was performed by blinded investigators using the Cell Counter tool and Threshold + the Analyze Particles tool in Fiji Is Just ImageJ (Fiji).[34] When automatically quantifying cell size and morphology with the Analyze Particles tool, a particle area of 50 μm^2 was used as the lower cutoff for cell size to exclude background speckles. Quantification of human astrocyte cell morphology was performed by blinded investigators manually outlining individual cells using Polygon Selections + the Measure tool in Fiji.

Western blot analysis of cultures

Four days after plating on CytoSoft substrates, cells were lysed in Mammalian Protein Extraction Reagent (M-PER) (Thermo Scientific) supplemented with HALT protease inhibitor cocktail (Thermo Scientific). Cellular debris was removed by centrifugation at 21,100 g for 10 min at 4°C and protein concentration was determined by bicinchoninic acid (BCA) assay (Thermo Scientific) with a standard curve of bovine serum albumin (BSA). Protein lysates were combined with Laemmli buffer containing 2-mercaptoethanol and boiled at 95°C for 10 min before loading. Samples were resolved with SDS-PAGE, transferred to Immobilon-P membranes (Millipore), and blocked with 5% milk. Primary and secondary antibodies used are listed in Supplementary Table S4. Blots were developed on Amersham Hyperfilm ECL (GE Healthcare) using ECL Western Blotting Substrate (Thermo Scientific). Membranes were stripped and re-probed with Restore Western Blot Stripping Buffer (Thermo Scientific). Films were scanned using a CanoScan 9000F scanner (Canon) and quantified using the Analyze Gels tool in Fiji.

Computational quantification of glial process alignment

Confocal image stacks were acquired from midsagittal spinal cord sections co-stained with glial fibrillary acidic protein (GFAP) and fibronectin using a 40 × oil immersion objective. (see Supplementary Table S4 for a list of antibodies used.) Image stacks were opened in Fiji and pre-processed with the Max Intensity Z-Projection and Split Channels tools to isolate the GFAP channel. The resulting images were imported into CurveAlign software (https://loci.wisc.edu/software/curvealign).[35] Individual fiber overlay visualizations were generated using the CT-FIRE module. Alignment heatmaps and curvelet overlay visualizations were generated using the default Curvelets Fiber Representation (CFR) mode. Foursquare 128 × 128 pixel regions of interest (ROIs), approximately 50 μm × 50 μm, were chosen per confocal image (four images per mouse) by a blinded investigator. These ROIs were selected along the GFAP$^+$ lesion rim to contain astrocytes that are in direct contact with the fibronectin$^+$ fibrotic scar core. CurveAlign automatically calculated the mean curvelet angle and alignment coefficient for each image and ROI. The alignment coefficient is a normalized, unitless, measure of fiber alignment with possible values between 0 (perfectly random fiber orientation) and 1 (perfect alignment).

Statistical analyses

All data are presented as means ± standard error of the mean (SEM). In box and whisker plots, the box indicates the 25th and 75th percentiles of the values, the line inside the box is the median value, and the whiskers the smallest and largest values. GraphPad Prism software (versions 5.04 and 8.0.1) was used to perform

statistical analysis of the data and a pre-determined significance level of $p < 0.05$ was used. No outlier values were excluded from any experiments. For AFM experiments, non-parametric Mann-Whitney and Kruskal-Wallis (Dunn's multiple comparison) tests were used to compare two and multiple groups, respectively. For the other experiments, two-group comparisons were performed using Student's *t* test. Multiple group comparisons used analysis of variance (ANOVA) with Tukey's post hoc test.

Data availability

The data presented in this study are available from the corresponding author upon request.

Results

Mechanical characterization of uninjured mouse spinal cord

We first investigated the mechanical properties of uninjured mouse spinal cords (12 weeks post-sham injury) using AFM (Fig. 2A). The average elastic modulus was determined to be 404 Pa for white matter and 405 Pa for gray matter (Fig. 2B) with no significant difference between the tissue types ($p = 0.9774$). No significant differences in the stiffness of white or gray matter were identified between individual animals (Supplementary Fig. S1).

To observe the spatial distribution of elasticity from uninjured spinal cord tissue, we performed AFM microindentation in a grid pattern and generated complete stiffness maps for white and gray matter. Figure 2E shows two representative stiffness maps with color indicating the gradient of elastic modulus observed spatially on white matter and gray matter regions (Supplementary Table S3). We observed no significant mechanical difference between the two maps ($p = 0.6137$, Supplementary Table S5), which is consistent with our previous results presented in Figure 2B. Thus spatially, the uninjured spinal cord tissue stiffness is relatively homogeneous with low variation of elastic values (Supplementary Table S3).

Spinal cord tissue stiffens chronically after contusion SCI

To investigate the mechanical properties of the chronically injured spinal cord, mice were subjected to a severe T11 contusion injury, and we assessed changes in tissue elasticity at 12 WPI. Our clinically relevant severe contusion injury model produces an irregular pattern of scarring with significant architectural disruption of the lesion site (Fig. 2C). Within the lesion core it is often impossible to clearly delineate tissue landmarks and gray versus white matter. For our analysis of injured spinal cord elasticity, we defined two tissue regions based on microscopic inspection of unstained

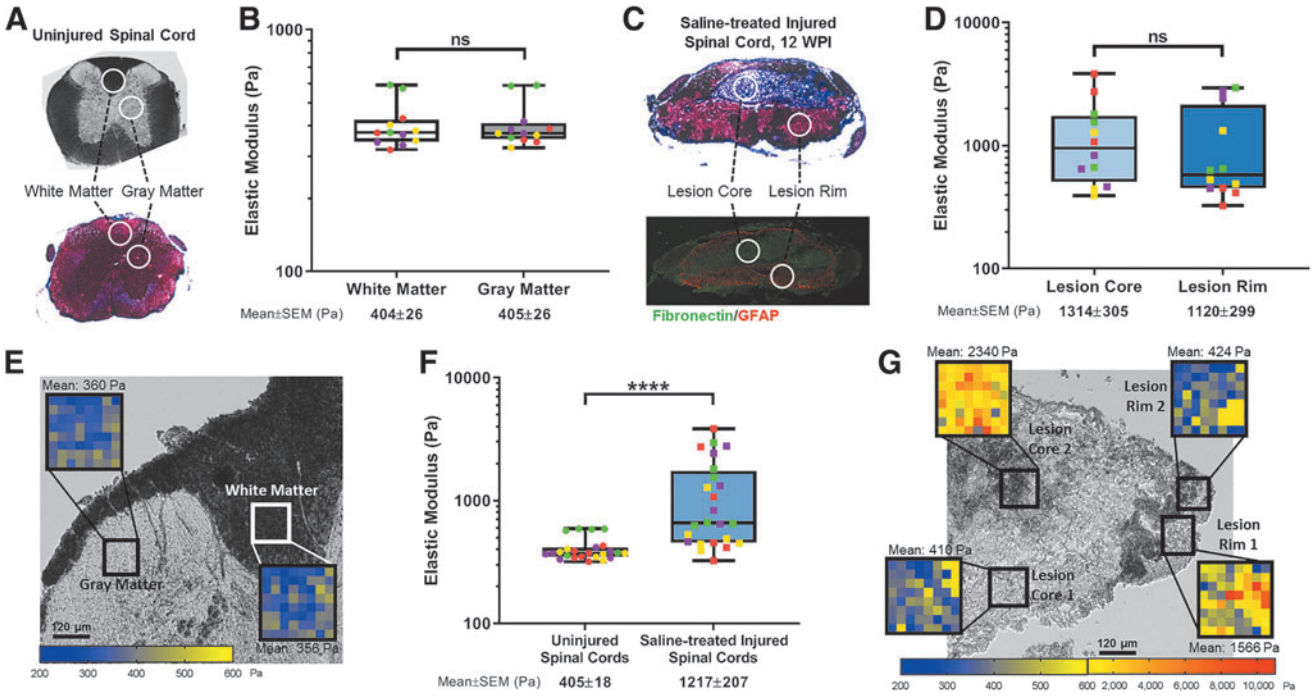

FIG. 2. Chronic stiffening of the spinal cord after contusion SCI. **(A)** Transverse sections from control uninjured (12 weeks post-sham injury) mouse spinal cords. Unstained (top), H&E stain (bottom) **(B)** There was no significant difference in elastic moduli of white and gray matter in uninjured (12 weeks post-sham injury) mouse spinal cords ($p = 0.9774$, Mann-Whitney test). **(C)** Transverse sections from injured (12 weeks post-severe contusion, saline-treated) mouse spinal cord. H&E stain (top), fibronectin and GFAP immunohistochemistry (bottom). **(D)** No statistical difference between the elastic moduli of lesion core and lesion rim regions of injured, saline-treated, spinal cords (12 WPI). **(E)** Stiffness maps of white and gray matter on uninjured spinal cord tissue. **(F)** Chronically injured spinal cord tissue (12 WPI) was significantly stiffer than uninjured tissue, including all regions (white and gray matters, lesion core and rim) (****$p < 0.0001$, Mann-Whitney test). **(G)** Stiffness maps of two different lesion core and rim areas on injured, saline-treated, spinal cord tissue (12 WPI). In box and whisker plots, the box indicates the 25th and 75th percentiles of the values, the line inside the box is the median value, and the whiskers the smallest and largest values. The color of each marker (B,D,F) identifies the individual mouse from which the sample was taken. For stiffness maps (E,G) each colored pixel represents the elastic modulus value measured at that point on the corresponding image according to the scale below. 12 WPI, 12 weeks post-injury; GFAP, glial fibrillary acidic protein; H&E, hematoxylin and eosin; SCI, spinal cord injury.

transverse sections. The ''lesion core'' region corresponds to the densely compacted fibronectin$^+$ region at the center of the injury. The ''lesion rim'' region corresponds to the GFAP$^+$ glial border area that surrounds and confines the lesion core (Fig. 2C).

AFM stiffness measurements showed that the lesion core and lesion rim regions have elastic moduli at 1314 and 1120 Pa, respectively (mean values, $n = 12$) (Fig. 2D). No significant difference was observed between these two lesion regions ($p = 0.4428$). Similarly, analyzing the same results on a per-animal basis showed no significant difference between lesion core and rim (Supplementary Fig. S2). Combining white and gray matter for control uninjured spinal cord tissue, and lesion core and rim for injured spinal cords, our results revealed significantly stiffer tissue at the lesion site 12 WPI (Fig. 2F, $****p < 0.0001$). A complete statistical analysis per region and condition is presented in Supplementary Table S6, and this highlights the significant differences. The lesion core contains fibrotic scar components such as fibronectin (Fig. 1C), and this observation in combination with the widely observed phenomenon of fibrosis-associated tissue stiffening in non-central nervous system (non-CNS) tissues,[36–38] led us to hypothesize that chronic spinal tissue stiffening after SCI is due to the presence of the fibrotic scar.

To analyze the relative spatial heterogeneity of elastic modulus in our SCI model, two stiffness maps were performed per regions (lesion core and rim) as previously described (Fig. 2G). We observed substantial spatial heterogeneity (mean elastic values) both across and within these maps (significant difference, Supplementary Table S5). For example, on the same tissue section, lesion core 2 area (mean elastic value: 2340 Pa) is significantly stiffer than lesion core 1 (410 Pa), whereas lesion rim 1 (1566 Pa) is significantly stiffer than lesion rim 2 (424 Pa), with no systematic relationship between stiffness and location within lesion rim and core. Even within local regions, we observe dramatic differences in modulus at the injury site. For example, elastic modulus values in lesion rim 1 span a range of $\sim$200 to $\sim$10,000 Pa (Supplementary Table S3), demonstrating dramatic variations from normal to highly stiffened. Taken together these results demonstrate the profound and heterogeneous stiffening of spinal cord tissue at 12 weeks post-severe-contusion injury.

Physiologically relevant changes in substrate stiffness alter astrocyte phenotype in vitro

Prior studies demonstrated that the stiffness of the extracellular environment can be an important determinate of glial cell growth and function.[9,39] However, these studies compared large and multiple orders of magnitude differences in elastic moduli between ''soft'' and ''hard'' substrates. We sought to determine whether changing substrate stiffness over the specific, physiologically relevant, range of compliances we observed in uninjured and chronically scarred spinal cord alter glial phenotype.

Primary mouse cortical astrocytes were plated onto PDL-coated, CytoSoft plates with elastic moduli of 200 Pa or 2000 Pa to mimic the rigidity of uninjured and chronically scarred spinal cord, respectively. A recent publication by Wilson et al. confirmed that CytoSoft substrates of various stiffness are uniformly coated by poly-L-lysine, reassuring us that any observed phenomenon are not a result of heterogenous coating of adhesion sites.[33] Cells were fixed and stained 4 days after plating. Striking morphological differences were immediately apparent between astrocytes cultured on 2000 Pa and 200 Pa plates (Fig. 3A). Astrocytes on the stiffer 2000 Pa ''scar'' substrate appear larger with multiple distinct processes, whereas astrocytes on the softer 200 Pa substrate appear smaller and more rounded. Some cells on the softer substrate display a ''fried egg'' appearance in which the cell is attached to the substrate, but no major processes extend from the cell body. Examination of F-actin structure using a phalloidin stain revealed the presence of actin stress fibers in the astrocytes (Fig. 3B). In cells grown on the scar-stiffness substrates, abundant stress fibers were aligned primarily along the major axes of the astrocyte cell bodies and extended into the feathery ends of the processes. Astrocytes grown on the softer substrate displayed only weakly filamentous staining patterns, with far fewer aligned actin stress fibers.

Morphometric analysis was performed using Fiji to quantify differences in astrocytic morphology. Astrocytes on the stiffer substrate demonstrated significantly increased surface area and decreased circularity compared with cells on the softer substrate (Fig. 3C,D; $*p < 0.05$ and $***p < 0.001$, respectively). To further quantify the differences in the morphologies, we performed manual classification according to the number of major processes, or ''arms,'' extending from each astrocyte. The distribution of process frequency was strikingly dependent on substrate rigidity (Fig. 3E, $****p < 0.0001$). The stiffer substrate material encouraged astrocytes to develop more complicated morphologies with both longer and more numerous processes.

Physiological changes in substrate stiffness alter mechanotransduction signaling in astrocytes in vitro

Integrin-mediated focal adhesions are a transmembrane linkage through which cells sense and exert tension on their mechanical environment.[5] Focal adhesions provide anchor points for F-actin bundles that mediate cellular cytoskeletal interactions with the ECM.[40,41] In light of the differential formation of actin stress fibers observed above (Fig. 3B), we examined whether changing substrate stiffness over their physiological range of uninjured/injured spinal cord alters expression of proteins associated with integrin-mediated mechanotransduction signaling pathways. Western blotting demonstrated significant increases in levels of β1-integrin and integrin-linked kinase (ILK) protein levels on scar-hard substrates compared with softer, uninjured-stiffness, substrates (Fig. 3F,G). GFAP, a classic marker of glial cell reactivity, increases significantly at the lesion site of injured spinal cord tissue at both acute and chronic time-points.[42,43] However, GFAP protein expression was not altered by changing substrate stiffness over the physiological range of uninjured/chronically injured spinal tissue (Fig. 3F,G).

Substrate stiffness alters phenotype of human-derived astrocytes

To our knowledge, no study has directly measured the mechanical properties of chronically injured human spinal cord tissue. Lacking that primary data, we believe that the mechanical properties of injured murine spinal cord may provide a reasonable first approximation of the mechanical environment within the injured human spinal cord. The effects of substrate rigidity on human astrocytes have not been previously reported, and it is possible that human glia do not respond to mechanical stimuli over the same range as murine cells. Therefore, to extend the clinical relevance of our findings, hESC-derived astrocytes were plated onto 200 Pa and 2000 Pa CytoSoft plates, and the cells were fixed and stained 5 days after plating.

Like the murine astrocytes, human astrocytes on the stiffer 2000 Pa substrate displayed prominent phalloidin-positive actin stress fibers not observed on the softer 200 Pa substrate (Fig. 4A,B). Also

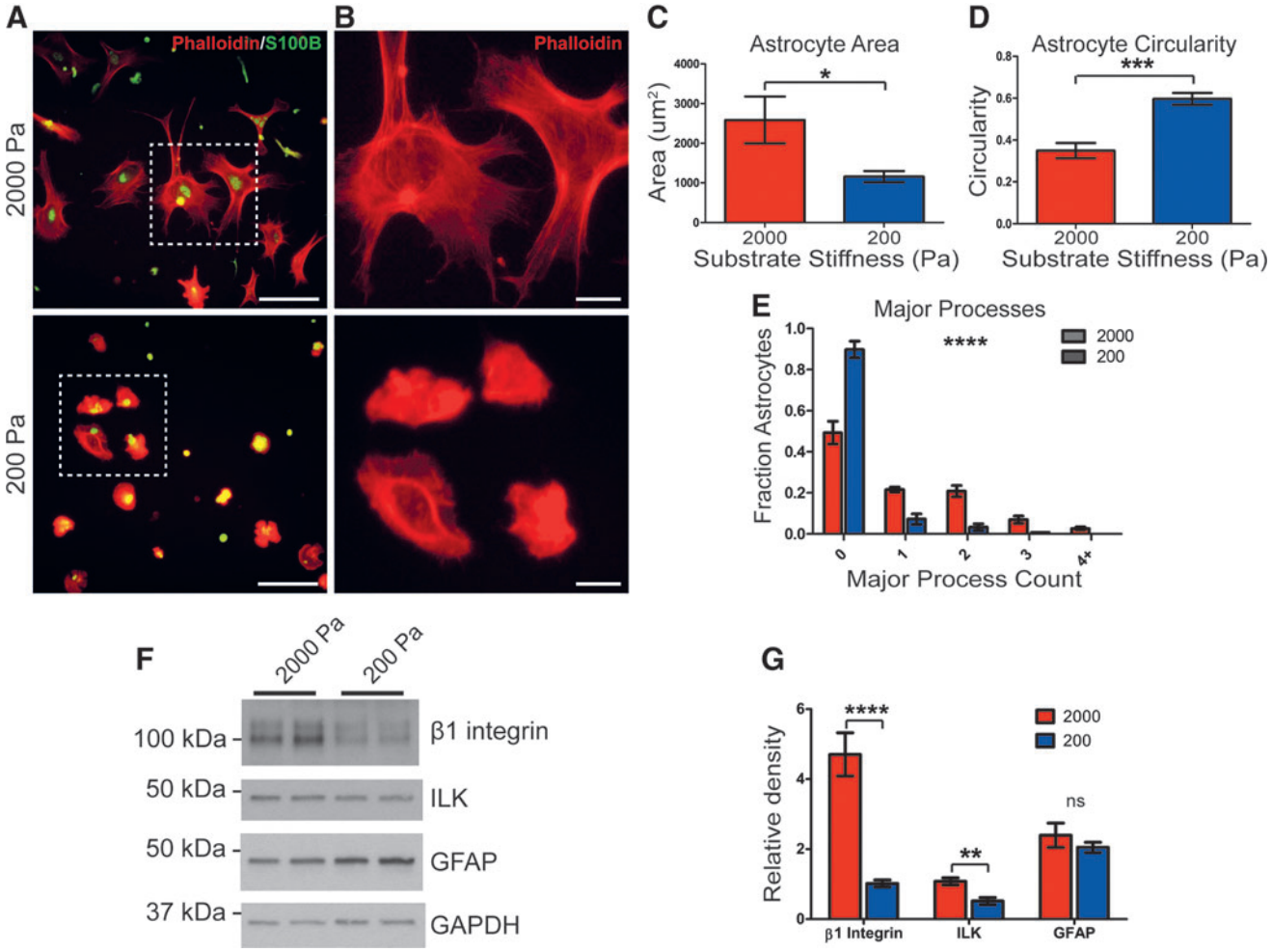

FIG. 3. Scar-stiffness substrates induce complex morphologies in cultured mouse astrocytes. **(A)** Representative images of murine astrocytes cultured for 4 days on scar stiffness (2000 Pa: top) or intact-tissue stiffness (200 Pa: bottom) stained for actin (phalloidin) and S100ß. Scale bar = 100 μm. **(B)** Enlarged images of the outlined areas demonstrate actin stress fibers. Scale bar = 25 μm. Astrocytes cultured on the stiffer 2000 Pa substrate demonstrate **(C)** increased surface area and **(D)** decreased circularity ($n = 6$ culture replicates, two-tailed Student's t test). **(E)** Stiffer culture substrates result in the extension of more numerous processes or ''arms'' ($n = 6$ culture replicates, two-way ANOVA). **(F, G)** Western blot analysis shows significantly reduced levels of mechanosensitive signaling molecules ß1-integrin and ILK in astrocytes cultured on soft (200 Pa) as compared with stiff (2000 Pa) substrate. GFAP expression is unchanged. ($n = 5$–7 culture replicates, two-tailed Student's t test) $^{*}p < 0.05$, $^{**}p < 0.01$, $^{***}p < 0.001$, $^{****}p < 0.0001$. Error bars are SEM. ANOVA, analysis of variance; GFAP, glial fibrillary acidic protein; ILK, integrin-linked kinase; SEM, standard error of the mean.

like murine astrocytes, human astrocytes grown on the stiffer 2000 Pa substrate demonstrated decreased circularity as compared with those grown on the softer substrate (Fig. 4D, $^{**}p < 0.01$). However, the surface area of human astrocytes was not affected by substrate stiffness over the range studied (Fig. 4C). Quantification of morphological complexity according to the number of major processes extending from each astrocyte revealed a significant shift toward more complex morphologies on the stiffer substrate. (Fig. 4E, $^{****}p <$ 0.0001). Thus mouse and human astrocytes display similar morphological responses to a changing mechanical environment. Stiffer environments encourage astrocytes to assume more complex shapes and extend more numerous processes into their surroundings.

IMP treatment rescues chronic stiffening of spinal tissue after contusion SCI

Our group has previously demonstrated that acute intravenous treatment with IMP after SCI selectively reduces chronic fibrotic scarring in mice.[14] This therapy works by markedly limiting infiltration of circulating monocytes/macrophages into the injury site with reduction in the acute expression of cytokines/chemokines within the lesion. IMP treatment results in a durable attenuation of the chronic fibrotic scar and improvement in motor function for up to at least 8 months post-injury (Jeong et al.[14] and Fig. 5A). To determine the effects of reducing fibrotic scarring on the mechanical properties of the chronically injured spinal cord tissue, mice were treated with intravenous IMP or vehicle at 2, 24, and 48 h after the contusion injury. AFM microindentation was then used to examine tissue elasticity at 12 WPI.

The overall stiffness of lesion site (core and rim combined) after IMP treatment (517 Pa) is significantly lower than for saline treatment (1217 Pa, $^{*}p = 0.018$), and close to elastic results for uninjured spinal cord tissue (405 Pa, no significant difference, $p = 0.0711$) (Fig. 5B). Detailed statistical analyses per region for all three conditions are presented in Supplementary Table S6 and reveal a significant reduction of lesion core stiffness for mice treated

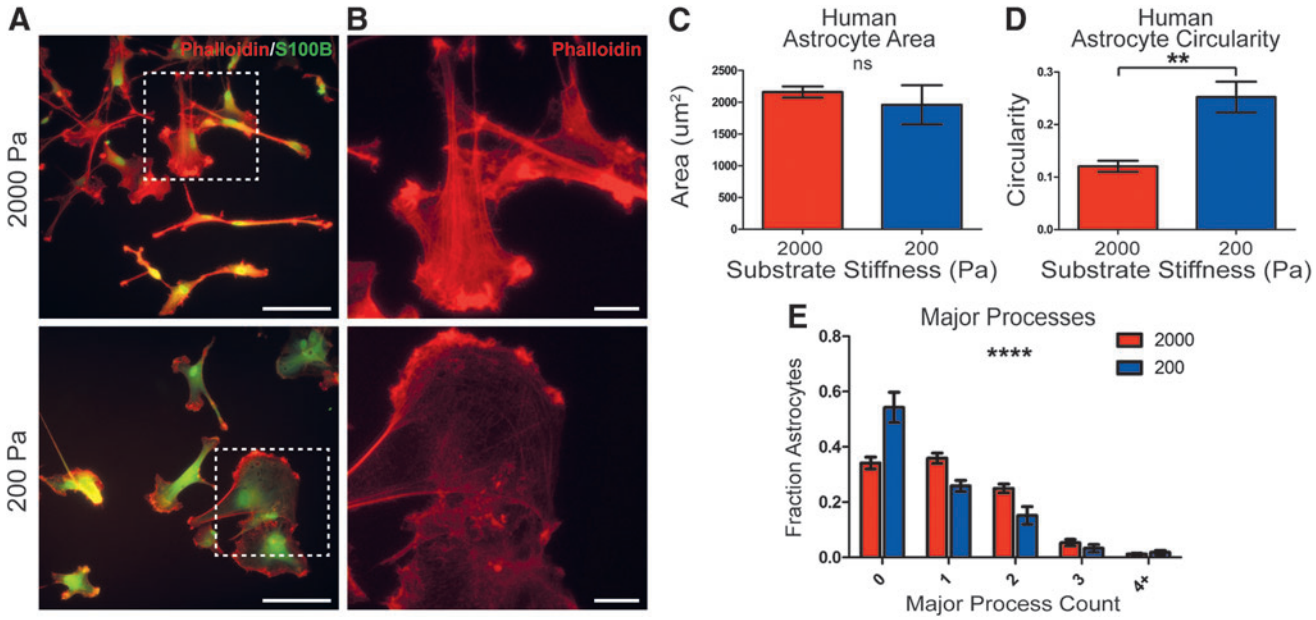

FIG. 4. Cultured human astrocytes respond to substrate-stiffness cues. **(A)** Representative images of hESC-derived astrocytes cultured for 5 days on scar stiffness (2000 Pa: top) or intact-tissue stiffness (200 Pa: bottom) stained for actin (phalloidin) and S100ß. Scale bar = 100 μm. **(B)** Enlarged images of the outlined areas demonstrate actin stress fibers. Scale bar = 25 μm. Astrocytes cultured on the stiffer 2000 Pa substrate show **(C)** no change in surface area but **(D)** demonstrate decreased circularity ($n = 5$ culture replicates, two-tailed Student's t test). **(E)** Stiffer culture substrates result in the extension of more numerous processes or ''arms'' ($n = 5$ culture replicates, two-way ANOVA). $^{**}p < 0.01$, $^{****}p < 0.0001$. Error bars are SEM. ANOVA, analysis of variance; hESC, human embryonic stem cell; SEM, standard error of the mean.

with IMP at 12 WPI compared with saline treatment ($^{*}p = 0.0144$). The lesion rim area (601 Pa) is significantly stiffer than lesion core (434 Pa) after IMP treatment (Fig. 5C, $^{*}p = 0.0432$; results per each animal in Supplementary Fig. S3). The stiffness maps performed on injured spinal cord tissue and treated with IMP (Fig. 5D) show intermediate elastic moduli values and ranges compared with values obtained with uninjured and injured, saline treated, spinal tissue samples (Supplementary Table S3).

IMP treatment alters glial fiber alignment within the chronic spinal scar.

We previously found that IMP treatment did not affect GFAP protein expression, as assessed by both immunohistochemistry (IHC) and western blot,[14] suggesting that IMP treatment selectively attenuated fibrotic scarring without inhibiting glial scarring. However, because we found that astrocytes *in vitro* respond to the mechanical environments by altering their morphology without altering expression of GFAP protein (Fig. 4F,G), we explored the possibility that the mechanically softer environment of the IMP-treated spinal cord might result in morphological changes in astrocytes in the glial scar that were not assessed by a simple analysis of GFAP levels.

In the chronically injured spinal cord, GFAP^{+} astrocytic processes are woven together into a complex meshwork that limits the ability to outline single astrocytes within the glial scar for morphological analysis of individual cells. Therefore, we quantified the structural alignment characteristics of the glial scar latticework using CurveAlign, a curvelet-based analysis program developed for quantification of fiber alignment. CurveAlign provides a normalized, unitless, measure of fiber alignment called the alignment coefficient based on a curvelet transform representation of an image.[44] The alignment coefficient has possible values between 0 (perfectly random) and 1 (perfectly aligned).

Using CurveAlign, we quantified the fibrillar alignment of GFAP^{+} processes in uninjured spinal cords and within regions of interest along the glial rim region of chronically injured (12 WPI) spinal cords (Fig. 6A–D). Regions of interest from injured cord sections were selected to contain astrocytes that directly contact the fibronectin^{+} fibrotic scar core. Injured, saline-treated, mice at 12 WPI displayed a highly aligned, anisotropic, network of GFAP^{+} astrocytic processes along the glial/fibrotic scar interface. The GFAP fibrillary alignment in these mice was significantly greater that that observed in uninjured control spinal cords. Cage-mate 12 WPI mice that received acute IMP treatment displayed a more isotropic astrocyte topology, indicated by smaller alignment coefficients (Fig. 6E, $^{**}p < 0.01$). Further, there was no significant difference in glial fiber alignment coefficients between IMP-treated mice and uninjured controls at 12 WPI, although the IMP-treated mice did trend higher.

Discussion

This study examined the effects of a severe contusion SCI on the stiffness of spinal cord tissue in chronically injured mice and demonstrated that spinal scars are stiffer than normal tissue. Scar tissue throughout the body is typically stiffer than the surrounding healthy tissue.[36–38] By analogy, it had long been assumed that spinal lesions are stiffer than uninjured spinal tissue, creating a mechanical blockade to neuronal regeneration.[6,8,10] However, prior to our study there has not been experimental evidence supporting the widespread assumption that spinal scars after SCI are stiffer than healthy tissue, and some recent studies have challenged this

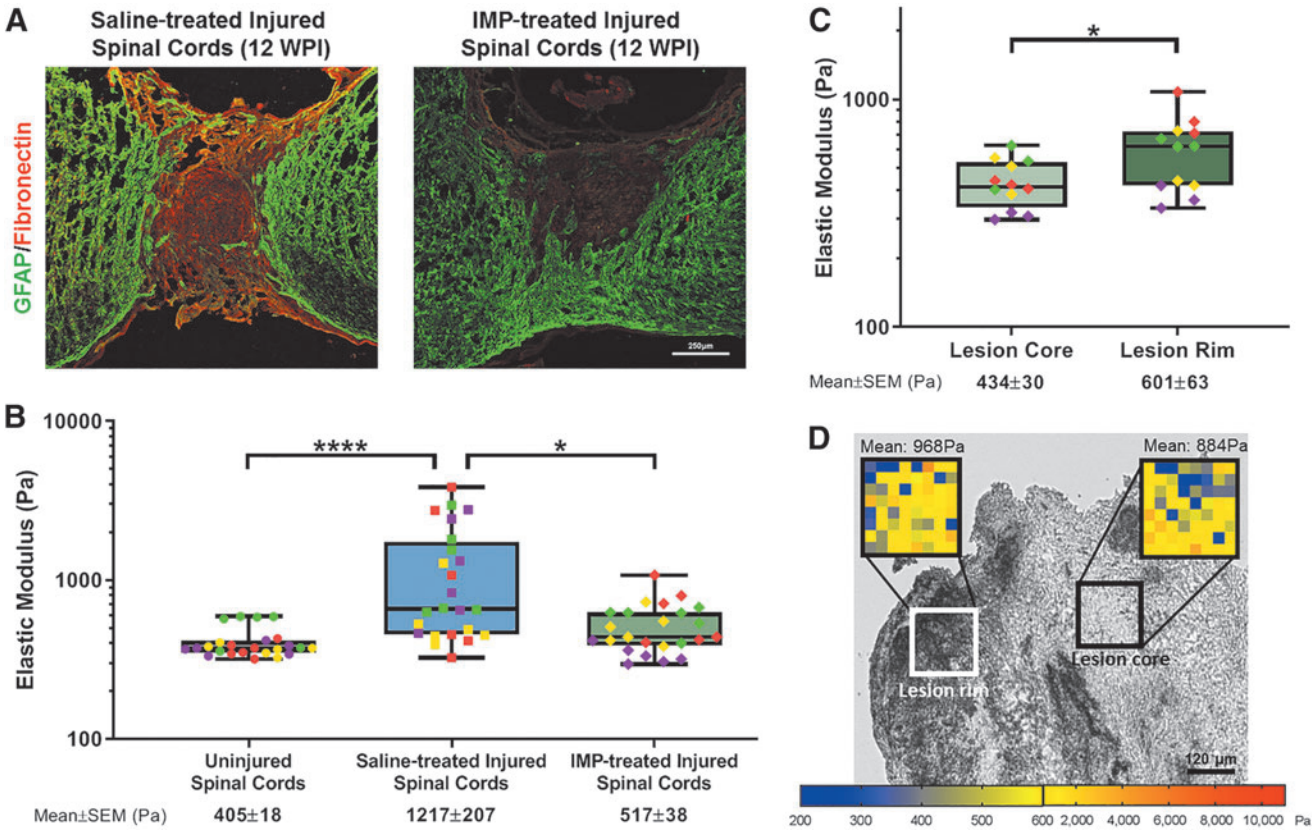

FIG. 5. IMP treatment after SCI rescues chronic tissue stiffening. **(A)** Mid-sagittal sections from 12 WPI IMP- or saline-treated mice stained for fibronectin and GFAP. Scale bar = 250 μm. **(B)** Mice who received IMP treatment after injury have significantly softer lesion sites than their saline treated counterparts (*$p = 0.0180$, Kruskal-Wallis test). There was no significant difference in elastic moduli between uninjured spinal cord and the IMP-treated lesion site at 12 WPI. **(C)** Spinal lesion rim regions are stiffer than lesion core regions in IMP-treated mice (12 WPI) (*$p = 0.0432$, Mann-Whitney test). **(D)** Stiffness maps of lesion core and rim regions on injured, IMP-treated, spinal cord tissue (12 WPI). In box and whisker plots, the box indicates the 25th and 75th percentiles of the values, the line inside the box is the median value, and the whiskers the smallest and largest values. The color of each data point identifies the individual mouse from which the sample was taken. *$p < 0.05$, ****$p < 0.0001$. 12 WPI, 12 weeks post-injury; GFAP, glial fibrillary acidic protein; IMP, immune modifying nanoparticle; SCI, spinal cord injury;

view. For example, Moeendarbary et al. demonstrated a softening of spinal tissue 1–3 weeks after a forceps crush injury in rats,[11] and they concluded that in contrast to scars in other mammalian tissues, CNS tissue significantly softens after injury. This acute loss of mechanical stiffness agrees with reports that acute inflammation is associated with decreased brain tissue stiffness in a mouse model of experimental autoimmune encephalomyelitis.[45] In acute and subacute lesions, fibroblasts have infiltrated the lesion site, but the dense extracellular meshwork of assembled-fibronectin that characterizes the chronic fibrotic scar has yet to be fully established.[46] Thus, the acute softening of the lesion site in the study by Moeendarbary et al. likely reflects the acute inflammatory reaction that occurs after SCI, whereas the chronic stiffening that we observed reflects scar formation.

The elastic moduli we report for uninjured mouse spinal cord agree closely with previously published values that were also determined using the AFM microindentation technique along the rostral-caudal axis and analyzed using the Hertz spherical indentation model.[5,11] We have also demonstrated that spinal cord mechanical properties are not affected by the frozen/thawing sample preparation process. These values for uninjured spinal cord are softer than the elastic modulus of uninjured rat cord reported by Saxena et al.[12] ($\sim$1250 Pa). However, that study utilized a compressive indentation method in which the cord was compressed along the dorsal-ventral axis with a tip 2 orders of magnitude wider in diameter than ours and analyzed using a different mathematical modeling method.[12] Our group has previously found that the size of AFM tip and the thickness of tissue section have an important influence on the measured elastic modulus of pulmonary arterial tissue.[19]

Koser et al. also reported that the measured mechanical properties of the spinal cord are highly dependent upon the anatomical plane along which the measurements are conducted.[14] Indeed, in this study we have observed the influence of the forces applied during measurement of spinal cord mechanical properties. However, the lack of published literature systematically comparing experimental techniques, size of indenter, AFM parameters, animal species, and sample thickness is a current limitation. We consider that the discrepancies in reported elastic moduli for uninjured spinal cord tissue is most likely due to these methodological differences.

The current literature does not give a consistent picture of stiffness differences between white and gray matter in the brain and spinal cord. Many studies, utilizing a variety of experimental

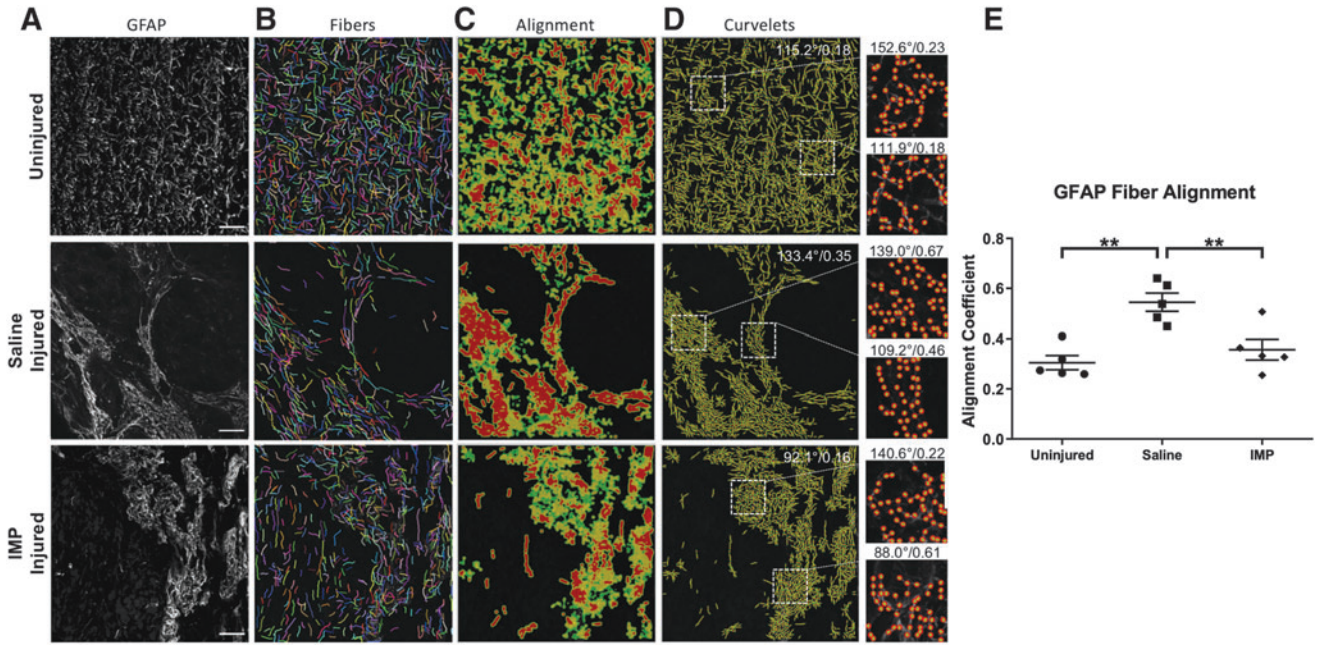

FIG. 6. IMP treatment alters glial fiber alignment in the chronic glial scar. **(A)** The GFAP-positive astrocytic fiber network is visualized along the glial/fibrotic interface using traditional immunohistochemistry at 12 WPI. Scale bar = 50 μm. **(B)** Visualization of extracted individual fibers using CurveAlign CT-FIRE mode overlaid on the IHC image. **(C)** A heatmap view of curvelet alignment. Red coloring indicates areas with high alignment. **(D)** Curvelet overlay visualization showing the location (red dots) and orientation (green lines) of individual curvelets computed using the CurveAlign curvelet fiber representation mode. Enlarged images illustrate outlined representative ROIs selected along the glial border region adjacent to the fibrotic core. Quantification results from large images and individual ROIs are displayed in the format: ''mean angle°/alignment coefficient'' at the top of each panel. **(E)** Quantification of GFAP-positive fiber alignment within ROIs along the glial border zone shows reduced glial alignment in IMP-treated tissue as compared with saline. There is no significant difference in alignment between uninjured and IMP-treated tissue. Each marker represents the mean alignment coefficient of 16 regions of interest from a single experimental animal. (four ROIs per image, four images per mouse) ($n = 5$ mice per group, one-way ANOVA with Tukey's post hoc test) $^{**}p < 0.01$. 12 WPI, 12 weeks post-injury; ANOVA, analysis of variance; GFAP, glial fibrillary acidic protein; IMP, immune modifying nanoparticle; ROI, region of interest.

methods, conclude that gray matter is stiffer than white matter.[11,16,47–50] Other studies have found the opposite, reporting that white matter is stiffer than gray.[51–53] Still other studies have failed to find any significant difference between the moduli of white and gray matter in CNS tissue.[54,55] This is a deceptively challenging question to answer because neural tissue is so complex, with anisotropic and inhomogeneous mechanical properties and significant variation between anatomical regions that lie only millimeters apart. Further, different experimental methods have unique strengths and limitations and operate at divergent length scales. This is a complex topic that has been reviewed by Cheng et al.[56] and Budday et al.[57] In the present work, we did not identify a significant difference in stiffness between gray and white matter in our spinal cord sections. This may be due also to the stringency of our statistical analysis, in which we regarded each region of interest as one, rather than each individual force curve and the low force applied in our measurement paradigm.

The study by Saxena et al. also reported that rat spinal tissue exhibits lower elastic modulus at both 2 and 8 weeks after a spinal hemisection injury.[12] In addition to the differences in sample preparation and indentation measurement methods discussed above, the hemisection injury model replicates only a small portion of the injuries observed in human patients.[1] It is likely that their hemisection injury and our contusion injury produce different scar environments, each of which displays a unique set of mechanical properties. Also, as noted above, their values for the elastic moduli in uninjured mouse spinal cord are much higher than those we observed and that have been reported previously[5,11] making it difficult to evaluate comparisons between injured and uninjured tissue.

The literature demonstrates that the stiffness of the extracellular environment influences glial behavior and function. However, most *in vitro* studies compare ''soft'' and ''hard'' substrates with multiple order-of-magnitude differences in elastic modulus that do not reflect the observed stiffness of actual CNS tissue.[9,39] Using variable stiffness cell culture substrates, we demonstrated that astrocytes undergo significant changes in morphology and mechanosensitive protein expression over the physiologically relevant range of elastic moduli observed in uninjured and chronically scarred murine spinal cords. We then used human-derived astrocyte cultures to confirm that human astrocytes respond in a similar way over the same physiological range of stiffnesses. Although the elastic modulus of the chronically injured human spinal cord has never been directly reported, we have used our measured stiffness values from the mouse spinal cord as an approximation. To our knowledge, this is the first study to examine the effect of substrate stiffness on cultured human astrocytes.

Fibrotic stiffening is a well-documented phenomenon in a wide variety of extra-CNS tissues.[36–38] Because we observed a trend toward a larger percentage increase in stiffness within the fibrotic lesion core region, we hypothesized that the increased elastic modulus of chronically injured spinal tissue is due, at least in part,

to the mature fibrotic scar. To test this hypothesis, we utilized IMP to reduce fibrotic scarring after SCI. A previously published study from our group showed that acute intravenous IMP treatment after SCI results in long-term reduction of both lesion size and fibrotic scarring but does not alter GFAP expression in the surrounding glial scar. IMP-treated animals also display significantly improved functional recovery after both moderate and severe SCI.[14] Here, acute IMP treatment successfully rescued the chronic stiffening of injured spinal cord. We failed to detect any significant difference in elastic moduli between uninjured spinal cord and injured, IMP-treated, lesion core at 12 WPI. PBS-treated animals did not show any difference in stiffness between lesion core and lesion rim. However, IMP treatment did result in a significant decrease in lesion core stiffness as compared with lesion rim. Because the lesion core contains the compacted fibrotic scar components, these results implicate fibrosis in the chronic tissue stiffening observed after SCI.

Although IMP treatment after SCI does not alter GFAP expression within the glial scar, it does make the environment softer. The results of our work *in vitro* on substrate stiffness encouraged us to examine the effects of IMP-induced scar softening on the topological complexity of the glial scar network around the lesion core. The glial border zone of a chronically injured spinal lesion consists of aligned sheets of $GFAP^+$ astrocytic processes. This configuration echoes the pathologically over-aligned collagen topology observed in the stroma surrounding some breast and pancreatic adenocarcinomas.[44,58] This similarity led us to borrow a quantitative fiber alignment analysis tool, CurveAlign, from the tumor biology world. Using CurveAlign we were able to demonstrate that chronic scarring after SCI leads to a highly aligned, anisotropic network of $GFAP^+$ astrocytic processes along the glial/fibrotic scar interface. Acute IMP treatment after injury resulted in a less aligned network of glial processes with higher isotropy that more closely resembles the astrocytic network in uninjured spinal cord.

The reduced complexity of the astroglial scar lattice observed *in vivo* in the mechanically softer, IMP-treated spinal cords echoes the reduced morphological complexity of astrocytes *in vitro* cultured on softer, healthy-tissue-stiffness substrates. Our AFM data demonstrated that astrocytes along the glial/fibrotic scar interface of IMP-treated spinal cords experience a more compliant mechanical environment than their untreated counterparts. Taken together, these results suggest that changes in 3D tissue stiffness within the injured spinal cord may participate in altering astrocytic phenotype and in maintenance of the chronic glial scar that is a hallmark of the injured mammalian spinal cord. This highly aligned network of astrocytes that forms within the glial scar also may contribute to stiffening of the mechanical environment. Thus, the mechanical properties of the lesion site are an important aspect of the complex lesion milieu that must be considered when assessing and developing potential clinical interventions for SCI.

Acknowledgments

We thank all members of the J.A.K and D.J.T. laboratories for their help and support. In particular the authors thank J.A. Meridew, P. Delmotte, I. Jorba, J. Varga, and C.Y. Peng for their consultation and critical support.

Funding Information

This research was supported by NIH, National Institute of Neurological Disorders and Stroke (NINDS) F30NS093811 (to J.G.C) and NIH, National Heart, Lung, and Blood Institute (NHLBI) 5RO1-HL-133320 (to D.J.T.).

Author Disclosure Statement

No competing financial interests exist.

Supplementary Material

Supplementary Figure S1
Supplementary Figure S2
Supplementary Figure S3
Supplementary Table S1
Supplementary Table S2
Supplementary Table S3
Supplementary Table S4
Supplementary Table S5
Supplementary Table S6

References

1. Bunge, R.P., Puckett, W.R., and Hiester, E.D. (1997). Observations on the pathology of several types of human spinal cord injury, with emphasis on the astrocyte response to penetrating injuries. Adv. Neurol. 72, 305–315.
2. Soderblom, C., Luo, X., Blumenthal, E., Bray, E., Lyapichev, K., Ramos, J., Krishnan, V., Lai-Hsu, C., Park, K.K., Tsoulfas, P., and Lee, J.K. (2013). Perivascular fibroblasts form the fibrotic scar after contusive spinal cord injury. J. Neurosci. 33, 13882–13887.
3. Hu, H.Z., Granger, N., Pai, S.B., Bellamkonda, R.V., and Jeffery, N.D. (2018). Therapeutic efficacy of microtube-embedded chondroitinase ABC in a canine clinical model of spinal cord injury. Brain 141, 1017–1027.
4. Bradbury, E.J., and Carter, L.M. (2011). Manipulating the glial scar: chondroitinase ABC as a therapy for spinal cord injury. Brain Res. Bull. 84, 306–316.
5. Franze, K., Janmey, P.A., and Guck, J. (2013). Mechanics in neuronal development and repair. Annu. Rev. Biomed. Eng. 15, 227–251.
6. Moshayedi, P., Costa, L.d.F., Christ, A., Lacour, S.P., Fawcett, J., Guck, J., and Franze, K. (2010). Mechanosensitivity of astrocytes on optimized polyacrylamide gels analyzed by quantitative morphometry. J. Phys. Condens. Matter 22, 194114.
7. Flanagan, L.A., Ju, Y.E., Marg, B., Osterfield, M., and Janmey, P.A. (2002). Neurite branching on deformable substrates. Neuroreport 13, 2411–2415.
8. Yu, X., and Bellamkonda, R.V. (2001). Dorsal root ganglia neurite extension is inhibited by mechanical and chondroitin sulfate-rich interfaces. J. Neurosci. Res. 66, 303–310.
9. Georges, P.C., Miller, W.J., Meaney, D.F., Sawyer, E.S., and Janmey, P.A. (2006). Matrices with compliance comparable to that of brain tissue select neuronal over glial growth in mixed cortical cultures. Biophys. J. 90, 3012–3018.
10. Windle, W.F., and Chambers, W.W. (1950). Regeneration in the spinal cord of the cat and dog. J. Comp. Neurol. 93, 241–257.
11. Moeendarbary, E., Weber, I.P., Sheridan, G.K., Koser, D.E., Soleman, S., Haenzi, B., Bradbury, E.J., Fawcett, J., and Franze, K. (2017). The soft mechanical signature of glial scars in the central nervous system. Nature Commun. 8, 14787.
12. Saxena, T., Gilbert, J., Stelzner, D., and Hasenwinkel, J. (2012). Mechanical characterization of the injured spinal cord after lateral spinal hemisection injury in the rat. J. Neurotrauma 29, 1747–1757.
13. Kilkenny, C., Browne, W.J., Cuthill, I.C., Emerson, M., and Altman, D.G. (2010). Improving bioscience research reporting: the ARRIVE guidelines for reporting animal research. PLoS Biol. 8, e1000412.
14. Jeong, S.J., Cooper, J.G., Ifergan, I., McGuire, T.L., Xu, D., Hunter, Z., Sharma, S., McCarthy, D., Miller, S.D., and Kessler, J.A. (2017). Intravenous immune-modifying nanoparticles as a therapy for spinal cord injury in mice. Neurobiol. Dis.108, 73–82.
15. Cooper, J.G., Jeong, S.J., McGuire, T.L., Sharma, S., Wang, W., Bhattacharyya, S., Varga, J., and Kessler, J.A. (2018). Fibronectin EDA forms the chronic fibrotic scar after contusive spinal cord injury. Neurobiol. Dis. 116, 60–68.

16. Koser, D.E., Moeendarbary, E., Hanne, J., Kuerten, S., and Franze, K. (2015). CNS cell distribution and axon orientation determine local spinal cord mechanical properties. Biophys. J. 108, 2137–2147.
17. Thundat, T., Allison, D.P., and Warmack, R.J. (1994). Stretched DNA structures observed with atomic force microscopy. Nucleic Acids Res. 22, 4224–4228.
18. Dimitriadis, E.K., Horkay, F., Maresca, J., Kachar, B., and Chadwick, R.S. (2002). Determination of elastic moduli of thin layers of soft material using the atomic force microscope. Biophys. J. 82, 2798–2810.
19. Sicard, D., Fredenburgh, L.E., and Tschumperlin, D.J. (2017). Measured pulmonary arterial tissue stiffness is highly sensitive to AFM indenter dimensions. J. Mech. Behav. Biomed. Mater. 74, 118–127.
20. Hertz, H. (1881). Über die Berührung fester elastischer Körper (On the contact of elastic solids). Journal für die reine und angewandte Mathematik 92, 156–171.
21. Harris, A.R., and Charras, G.T. (2011). Experimental validation of atomic force microscopy-based cell elasticity measurements. Nanotechnology 22, 345102.
22. Rico, F., Roca-Cusachs, P., Gavara, N., Farre, R., Rotger, M., and Navajas, D. (2005). Probing mechanical properties of living cells by atomic force microscopy with blunted pyramidal cantilever tips. Phys. Rev. E Stat. Nonlin. Soft Matter Phys.72, 021914.
23. Soucy, P.A., Werbin, J., Heinz, W., Hoh, J.H., and Romer, L.H. (2011). Microelastic properties of lung cell-derived extracellular matrix. Acta Biomater 7, 96–105.
24. Mahaffy, R.E., Shih, C.K., MacKintosh, F.C., and Käs, J. (2000). Scanning probe-based frequency-dependent microrheology of polymer gels and biological cells. Phys. Rev. Lett. 85, 880–883.
25. Gavara, N., and Chadwick, R.S. (2012). Determination of the elastic moduli of thin samples and adherent cells using conical atomic force microscope tips. Nature Nanotechnol. 7, 733–736.
26. Long, R., Hall, M.S., Wu, M., and Hui, C.Y. (2011). Effects of gel thickness on microscopic indentation measurements of gel modulus. Biophys. J. 101, 643–650.
27. Hayes, W.C., Keer, L.M., Herrmann, G., and Mockros, L.F. (1972). A mathematical analysis for indentation tests of articular cartilage. J. Biomech. 5, 541–551.
28. Finan, J.D., Fox, P.M., and Morrison, B., 3rd (2014). Non–ideal effects in indentation testing of soft tissues. Biomech. Model Mechanobiol. 13, 573–584.
29. Li, Q.S., Lee, G.Y., Ong, C.N., and Lim, C.T. (2008). AFM indentation study of breast cancer cells. Biochem. Biophys. Res. Commun. 374, 609–613.
30. Vishwakarma, S.K., Lakkireddy, C., Bardia, A., Paspala, S.A.B., and Khan, A.A. (2019). Engineering bio-mimetic humanized neurological constructs using acellularized scaffolds of cryopreserved meningeal tissues. Mater. Sci. Eng. C. Mater. Biol. Appl. 102, 34–44.
31. McCarthy, K.D., and de Vellis, J. (1980). Preparation of separate astroglial and oligodendroglial cell cultures from rat cerebral tissue. J. Cell Biol. 85, 890–902.
32. Wilson, C.L., Hayward, S.L., and Kidambi, S. (2016). Astrogliosis in a dish: substrate stiffness induces astrogliosis in primary rat astrocytes. RSC Adv. 6, 34447–34457.
33. Gutierrez, E., and Groisman, A. (2011). Measurements of elastic moduli of silicone gel substrates with a microfluidic device. PLoS One 6, e25534.
34. Schindelin, J., Arganda-Carreras, I., Frise, E., Kaynig, V., Longair, M., Pietzsch, T., Preibisch, S., Rueden, C., Saalfeld, S., Schmid, B., Tinevez, J.Y., White, D.J., Hartenstein, V., Eliceiri, K., Tomancak, P., and Cardona, A. (2012). Fiji: an open-source platform for biological-image analysis. Nat. Methods 9, 676–682.
35. Bredfeldt, J.S., Liu, Y., Pehlke, C.A., Conklin, M.W., Szulczewski, J.M., Inman, D.R., Keely, P.J., Nowak, R.D., Mackie, T.R., and Eliceiri, K.W. (2014). Computational segmentation of collagen fibers from second-harmonic generation images of breast cancer. J. Biomed. Opt. 19, 16007.
36. Wells, R.G. (2013). Tissue mechanics and fibrosis. Biochim. Biophys. Acta 1832, 884–890.
37. Wei, J., Bhattacharyya, S., Tourtellotte, W.G., and Varga, J. (2011). Fibrosis in systemic sclerosis: emerging concepts and implications for targeted therapy. Autoimmun. Rev. 10, 267–275.
38. Tjin, G., White, E.S., Faiz, A., Sicard, D., Tschumperlin, D.J., Mahar, A., Kable, E.P.W., and Burgess, J.K. (2017). Lysyl oxidases regulate fibrillar collagen remodelling in idiopathic pulmonary fibrosis. Dis. Model. Mech. 10, 1301–1312.
39. Moshayedi, P., Ng, G., Kwok, J.C., Yeo, G.S., Bryant, C.E., Fawcett, J.W., Franze, K., and Guck, J. (2014). The relationship between glial cell mechanosensitivity and foreign body reactions in the central nervous system. Biomaterials 35, 3919–3925.
40. Tojkander, S., Gateva, G., and Lappalainen, P. (2012). Actin stress fibers—assembly, dynamics and biological roles. J. Cell Sci. 125, 1855–1864.
41. Dupont, S. (2016). Role of YAP/TAZ in cell-matrix adhesion-mediated signalling and mechanotransduction. Exp. Cell Res. 343, 42–53.
42. Sofroniew, M.V. (2009). Molecular dissection of reactive astrogliosis and glial scar formation. Trends Neurosci. 32, 638–647.
43. Fawcett, J.W., and Asher, R.A. (1999). The glial scar and central nervous system repair. Brain Res. Bull. 49, 377–391.
44. Liu, Y., Keikhosravi, A., Mehta, G.S., Drifka, C.R., and Eliceiri, K. (2017). Methods for quantifying fibrillar collagen alignment, in: *Fibrosis. Methods in Molecular Biology*, vol. 1627. L. Rittié (ed). Humana Press: New York, pps. 429–451.
45. Riek, K., Millward, J.M., Hamann, I., Mueller, S., Pfueller, C.F., Paul, F., Braun, J., Infante-Duarte, C., and Sack, I. (2012). Magnetic resonance elastography reveals altered brain viscoelasticity in experimental autoimmune encephalomyelitis. Neuroimage Clin. 1, 81–90.
46. Zhu, Y., Soderblom, C., Trojanowsky, M., Lee, D.H., and Lee, J.K. (2015). Fibronectin matrix assembly after spinal cord injury. J. Neurotrauma 32, 1158–1167.
47. Ichihara, K., Taguchi, T., Shimada, Y., Sakuramoto, I., Kawano, S., and Kawai, S. (2001). Gray matter of the bovine cervical spinal cord is mechanically more rigid and fragile than the white matter. J. Neurotrauma 18, 361–367.
48. Elkin, B.S., Ilankovan, A.I., and Morrison, B., 3rd. (2011). A detailed viscoelastic characterization of the P17 and adult rat brain. J. Neurotrauma 28, 2235–2244.
49. Christ, A.F., Franze, K., Gautier, H., Moshayedi, P., Fawcett, J., Franklin, R.J., Karadottir, R.T., and Guck, J. (2010). Mechanical difference between white and gray matter in the rat cerebellum measured by scanning force microscopy. J. Biomech. 43, 2986–2992.
50. Prange, M.T., and Margulies, S.S. (2002). Regional, directional, and age-dependent properties of the brain undergoing large deformation. J. Biomech. Eng. 124, 244–252.
51. Kruse, S.A., Rose, G.H., Glaser, K.J., Manduca, A., Felmlee, J.P., Jack, C.R., Jr., and Ehman, R.L. (2008). Magnetic resonance elastography of the brain. Neuroimage 39, 231–237.
52. van Dommelen, J.A., van der Sande, T.P., Hrapko, M., and Peters, G.W. (2010). Mechanical properties of brain tissue by indentation: interregional variation. J. Mech. Behav. Biomed. Mater. 3, 158–166.
53. Budday, S., Nay, R., de Rooij, R., Steinmann, P., Wyrobek, T., Ovaert, T.C., and Kuhl, E. (2015). Mechanical properties of gray and white matter brain tissue by indentation. J. Mech. Behav. Biomed. Mater. 46, 318–330.
54. Finan, J.D., Elkin, B.S., Pearson, E.M., Kalbian, I.L., and Morrison, B., 3rd. (2012). Viscoelastic properties of the rat brain in the sagittal plane: effects of anatomical structure and age. Ann. Biomed. Eng. 40, 70–78.
55. Ozawa, H., Matsumoto, T., Ohashi, T., Sato, M., and Kokubun, S. (2001). Comparison of spinal cord gray matter and white matter softness: measurement by pipette aspiration method. J. Neurosurg. 95, 221–224.
56. Cheng, S., Clarke, E.C., and Bilston, L.E. (2008). Rheological properties of the tissues of the central nervous system: a review. Med. Eng. Phys. 30, 1318–1337.
57. Budday, S., Ovaert, T.C., Holzapfel, G.A., Steinmann, P., and Kuhl, E. (2019). Fifty Shades of Brain: A Review on the Mechanical Testing and Modeling of Brain Tissue. Arch. Comput. Methods Eng. https://doi.org/10.1007/s11831-019-09352-w (last accessed October 9, 2019).
58. Drifka, C.R., Tod, J., Loeffler, A.G., Liu, Y., Thomas, G.J., Eliceiri, K.W., and Kao, W.J. (2015). Periductal stromal collagen topology of pancreatic ductal adenocarcinoma differs from that of normal and chronic pancreatitis. Mod. Pathol. 28, 1470–1480.

Address correspondence to:
John A. Kessler, MD
Northwestern University
303 East Chicago Avenue
Chicago, IL 60611-3008

E-mail: jakessler@northwestern.edu